

## Response of a Stably Stratified Atmosphere to Low-Level Heating— An Application to the Heat Island Problem

JONG-JIN BAIK

*Universities Space Research Association, Laboratory for Atmospheres, NASA/Goddard Space Flight Center, Greenbelt, Maryland*

(Manuscript received 13 March 1991, in final form 31 July 1991)

### ABSTRACT

Two-dimensional airflow characteristics past a heat island are investigated using both a linear analytic model and a nonlinear numerical model in the context of the response of a stably stratified atmosphere to specified low-level heating in a constant shear flow. Results from the steady-state, linear, analytic solutions exhibit typical flow response fields that gravity waves produce in response to the local heat source in the presence of environmental flow. The magnitude of the perturbation vertical velocity is shown to be much larger in the shear-flow case than in the uniform-flow case. This is because the basic-state wind shear is a source of the perturbation wave energy.

Nonlinear numerical model experiments over a wide range of heating amplitudes are performed to examine nonlinear effects on the simulated flow field. For smaller heating amplitude (hence, smaller nonlinearity factor), the flow response field is similar to that produced by the linear gravity waves. On the other hand, two distinct flow features are observed for larger heating amplitude (hence, larger nonlinearity factor): the gravity-wave-type response field on the upstream side of the heat island and the strong updraft circulation cell located on the downstream side. As the heating amplitude increases, the updraft circulation cell strengthens and shifts farther downwind. The strong updraft cell is believed to be partly responsible for precipitation enhancement observed on the downstream side of the heat island. It is found that the continuing downwind propagation of the updraft circulation cell is related to basic-state wind speed.

### 1. Introduction

Air temperature near the surface in urban areas is usually higher than that in the surrounding rural areas because of larger surface heat capacity, lower daytime evaporation, anthropogenic heat input to the atmosphere, etc., in the urban region (e.g., Myrup 1969). This phenomenon, called the urban heat island, is especially pronounced at a night under clear skies when the synoptic wind is light (e.g., Oke 1973). A temperature contrast between a heated island and the surrounding sea also exists when the island is heated during the daytime.

The influence of a heat island on the atmospheric flow pattern, in either an urban or sea setting, can be studied theoretically in the context of the response of a stably stratified atmosphere to specified low-level thermal forcing. Olfe and Lee (1971) performed steady-state, linearized flow calculations in a uniform environmental flow to investigate urban heat island convection effects on temperature and velocity fields. The heat island forcing was represented by various surface temperature distributions. The results indicated positive temperature perturbations near the ground and

negative temperature perturbations aloft over urban areas, and downward motion directly over the upwind portion of the heat island and upward motion on the downstream side, which are consistent with observations (Angell et al. 1971; Garstang et al. 1975). Lin and Smith (1986) solved a time-dependent, linearized problem to study transient dynamics of the airstream near a local heat source of finite width and depth, which is turned on initially as a pulse or steadily in a uniform flow. The solutions were applied to several problems in mesoscale dynamics, including the heat island problem. They also found that air parcels descend over a heat island and ascend on the downstream side, and showed that the negative phase relationship between heating and vertical displacement in the vicinity of the heat source is directly related to the steadiness. Hsu (1987) examined steady-state, linear atmospheric responses to local surface heating of different scales in a constant mean horizontal wind. Under the assumption of constant stable temperature lapse rate and neglecting rotation, the scaled fourth-order ordinary differential equation was reduced to the heat island problem considered by Olfe and Lee (1971). In the studies by Olfe and Lee (1971) and Hsu (1987), solutions in physical space were obtained numerically from the fast Fourier transform of solutions in wavenumber space.

Recently, Lin (1987) studied the response of a shear flow to diabatic heating by solving a linearized problem with a wind-reversal level (or critical level). He pointed

---

*Corresponding author address:* Dr. Jong-Jin Baik, NASA/Goddard Space Flight Center, Universities Space Research Association, Severe Storms Branch (Code 912), Laboratory for Atmospheres, Greenbelt, MD 20771.

out the importance of the Richardson number and the nondimensional heating depth to the flow pattern. The critical level is often observed in the midlatitude squall lines in the reference frame of the moving lines (Ogura and Liou 1980). However, the existence of a critical level near a heat island is rare in the fixed frame of the heat island. In this paper, we will present an analytic model suitable for investigating airflow characteristics past a heat island. The model is similar to Lin's (1987) except that there is no wind-reversal level in a shear flow and the vertical heating function has a more realistic structure. Solutions in physical space will be obtained analytically.

Although the linearized studies mentioned above can provide some insight into the basic dynamics of the flow pattern past a heat island, the linear assumption breaks down as the low-level heating becomes stronger. To investigate transient behavior as well as nonlinearity, a time-dependent, nonlinear numerical model is developed. Observations (Changnon 1972; Changnon et al. 1991) indicate that precipitation is enhanced on the downstream side of a heat island. Even though this was partly attributed to the upward motion produced by the stationary heating of the heat island in the linear study by Lin and Smith (1986), we will present a more reasonable cause for precipitation enhancement downwind of the heat island through nonlinear numerical model simulations.

In section 2, a steady-state, linearized problem with diabatic heating in a stably stratified shear flow is solved analytically and the numerical model is described. In section 3, results from the steady-state, linear, analytic solutions and numerical model simulations are presented and discussed. Summary and conclusions are given in the last section.

## 2. Governing equations and solutions

Consider a two-dimensional, incompressible, hydrostatic, nonrotating, inviscid, Boussinesq airflow system. The governing equations for perturbation fields with basic-state horizontal wind and diabatic heating can be expressed by

$$\frac{\partial u}{\partial t} + U \frac{\partial u}{\partial x} + u \frac{\partial u}{\partial x} + w \frac{dU}{dz} + w \frac{\partial u}{\partial z} = - \frac{\partial \phi}{\partial x}, \quad (1)$$

$$\frac{\partial \theta}{\partial t} + U \frac{\partial \theta}{\partial x} + u \frac{\partial \theta}{\partial x} + w \frac{\partial \theta}{\partial z} + \frac{N^2 \theta_0}{g} w = \frac{\theta_0}{c_p T_0} q, \quad (2)$$

$$\frac{\partial u}{\partial x} + \frac{\partial w}{\partial z} = 0, \quad (3)$$

$$\frac{\partial \phi}{\partial z} = g \frac{\theta}{\theta_0}, \quad (4)$$

where

$t$  = time

$x$  = horizontal coordinate

$z$  = vertical coordinate

$u$  = perturbation wind speed in the  $x$  direction

$w$  = perturbation wind speed in the  $z$  direction

$\theta$  = perturbation potential temperature

$\phi$  = kinematic pressure perturbation ( $=p/\rho_0$ , where  $p$  is the perturbation pressure and  $\rho_0$  the basic-state density)

$U$  = basic-state wind speed in the  $x$  direction

$T_0$  = basic-state temperature

$\theta_0$  = basic-state potential temperature

$N$  = Brunt-Väisälä frequency

$g$  = gravitational acceleration

$c_p$  = specific heat of air at constant pressure

$q$  = heating function.

Equations (1)–(4) form a closed system in the unknowns  $u$ ,  $w$ ,  $\theta$ , and  $\phi$ . They are the momentum equation in the  $x$  direction, the thermodynamic energy equation, the mass continuity equation, and the hydrostatic equation, respectively. In this study, the basic-state horizontal wind speed is assumed to vary linearly with height.

$$U(z) = U_0 + sz \quad (U_0, s > 0), \quad (5)$$

where  $U_0$  is the wind speed at the surface and  $s$  the strength of the vertical wind shear. The heating function  $q$  is given by

$$q(x, z) = q_0 f(x) g(z), \quad (6)$$

where

$$f(x) = \frac{x_1^2}{x^2 + x_1^2} - \frac{x_1 x_2}{x^2 + x_2^2}, \quad (7)$$

$$g(z) = \begin{cases} 1 - \frac{z}{h} & \text{for } 0 \leq z \leq h \\ 0 & \text{for } z > h. \end{cases} \quad (8)$$

Here  $q_0$  is the amplitude of the heating function,  $x_1$  (half-width of the bell-shaped function) and  $x_2$  are constants with  $x_1 < x_2$ , and  $h$  is the height of the top of the heating zone. The second term on the right-hand side of Eq. (7) represents a widespread cooling term and is included to avoid the net heating problem (Smith and Lin 1982; Lin 1987) in a steady-state, linear, inviscid flow system. There is no net heating at any level because integration of  $q(x, z)$  from  $-\infty$  to  $\infty$  with respect to  $x$  is zero.

### a. Steady-state, linear, analytic solutions

Assuming steady-state and small-amplitude perturbation flow, Eqs. (1)–(4) are combined into a single equation for the perturbation vertical velocity

$$U^2 \frac{\partial^4 w}{\partial x^2 \partial z^2} + N^2 \frac{\partial^2 w}{\partial x^2} = \frac{g}{c_p T_0} \frac{\partial^2 q}{\partial x^2}. \quad (9)$$

Taking the Fourier transform ( $x \rightarrow k$ ) of Eq. (9), we get

$$(U_0 + sz)^2 \frac{\partial^2 \tilde{w}}{\partial z^2} + N^2 \tilde{w} = \frac{gq_0}{c_p T_0} \tilde{f}g(z). \quad (10)$$

The general solution of Eq. (10) is

$$\begin{aligned} \tilde{w}(k, z) = & A(k)(U_0 + sz)^{(1/2+ia)} \\ & + B(k)(U_0 + sz)^{(1/2-ia)} + \frac{gq_0}{c_p T_0 N^2} \tilde{f}\left(1 - \frac{z}{h}\right) \\ & \text{for } 0 \leq z \leq h, \end{aligned} \quad (11a)$$

$$\tilde{w}(k, z) = C(k)(U_0 + sz)^{(1/2+ia)}$$

$$+ D(k)(U_0 + sz)^{(1/2-ia)} \quad \text{for } z > h, \quad (11b)$$

where  $i = (-1)^{1/2}$  and  $a = (N^2/s^2 - 1/4)^{1/2} = (\text{Ri} - 1/4)^{1/2}$ . The Ri denotes the Richardson number defined by  $N^2/s^2$ , which is constrained to be larger than  $1/4$  in the present study. The coefficients  $A(k)$ ,  $B(k)$ ,  $C(k)$ , and  $D(k)$  can be determined by imposing proper upper radiation, lower boundary, and interface conditions. A radiation condition (Booker and Bretherton 1967) is used as an upper condition, which requires  $D(k) = 0$ . As a lower boundary condition, we set  $\tilde{w} = 0$  at  $z = 0$ . As interface conditions at  $z = h$ ,  $\tilde{w}$  and  $\partial \tilde{w} / \partial z$  are required to be continuous. Then, Eqs. (11a) and (11b) become

$$\begin{aligned} \tilde{w}(k, z) = & \frac{gq_0}{c_p T_0 N^2} \tilde{f} \left\{ \frac{i}{2ash} (U_0 + sh)^{(1/2+ia)} [(U_0 + sz)^{(1/2-ia)} - U_0^{-i2a} (U_0 + sz)^{(1/2+ia)}] + 1 \right. \\ & \left. - \frac{z}{h} - U_0^{(-1/2-ia)} (U_0 + sz)^{(1/2+ia)} \right\} \quad \text{for } 0 \leq z \leq h, \end{aligned} \quad (12a)$$

$$\begin{aligned} \tilde{w}(k, z) = & \frac{gq_0}{c_p T_0 N^2} \tilde{f} \left\{ \frac{i}{2ash} [(U_0 + sh)^{(1/2-ia)} - U_0^{-i2a} (U_0 + sh)^{(1/2+ia)}] - U_0^{(-1/2-ia)} \right\} (U_0 + sz)^{(1/2+ia)} \\ & \text{for } z > h. \end{aligned} \quad (12b)$$

After taking the inverse Fourier transform of Eqs. (12a) and (12b), a solution for  $w$  field is obtained.

$$\begin{aligned} w(x, z) = & \frac{gq_0 x_1}{c_p T_0 N^2} (U_0 + sz)^{1/2} \left[ \left( \frac{x_1}{x^2 + x_1^2} - \frac{x_2}{x^2 + x_2^2} \right) \left\langle E \{ \sin \alpha [\cos(y - 2\beta) - \cos y] \right. \right. \\ & + \cos \alpha [\sin(y - 2\beta) + \sin y] \} + (U_0 + sz)^{-1/2} \left( 1 - \frac{z}{h} \right) - U_0^{-1/2} \cos(y - \beta) \Bigg\rangle \\ & - \left( \frac{x}{x^2 + x_1^2} - \frac{x}{x^2 + x_2^2} \right) \left\langle E \{ \sin \alpha [\sin(y - 2\beta) + \sin y] + \cos \alpha [-\cos(y - 2\beta) + \cos y] \} \right. \\ & \left. \left. - U_0^{-1/2} \sin(y - \beta) \right\rangle \right] \quad \text{for } 0 \leq z \leq h, \end{aligned} \quad (13a)$$

$$\begin{aligned} w(x, z) = & \frac{gq_0 x_1}{c_p T_0 N^2} (U_0 + sz)^{1/2} \left[ \left( \frac{x_1}{x^2 + x_1^2} - \frac{x_2}{x^2 + x_2^2} \right) \left\langle E \{ \sin y [\cos(\alpha - 2\beta) - \cos \alpha] \right. \right. \\ & + \cos y [\sin(\alpha - 2\beta) + \sin \alpha] \} - U_0^{-1/2} \cos(y - \beta) \Bigg\rangle - \left( \frac{x}{x^2 + x_1^2} - \frac{x}{x^2 + x_2^2} \right) \\ & \left. \times \left\langle E \{ \sin y [\sin(\alpha - 2\beta) + \sin \alpha] + \cos y [-\cos(\alpha - 2\beta) + \cos \alpha] \} - U_0^{-1/2} \sin(y - \beta) \right\rangle \right] \\ & \text{for } z > h, \end{aligned} \quad (13b)$$

where

$$\begin{aligned} y &= a \ln(U_0 + sz) \\ E &= (2ash)^{-1} (U_0 + sh)^{1/2} \\ \alpha &= a \ln(U_0 + sh) \\ \beta &= a \ln U_0. \end{aligned}$$

The perturbation horizontal wind speed can be obtained analytically using Eqs. (3) and (13)

$$u(x, z) = - \int_{-\infty}^x \frac{\partial w}{\partial z} dx. \quad (14)$$

### b. Time-dependent, nonlinear, numerical solutions

Equations (1)–(4) are numerically solved on a rectangular, uniform, nonstaggered grid system. The first derivative term with respect to  $x$  is approximated by a fourth-order compact implicit scheme (Navon and Riphagen 1979) and the first derivative term with respect to  $z$  by a centered difference scheme. For the time marching, the Adams–Bashforth scheme with a second-order accuracy is used. A lower boundary condition of  $w = 0$  at  $z = 0$ , which is equivalent to the condition of  $\tilde{w} = 0$  at  $z = 0$  in the analytic solution part, is imposed.

Our system of governing equations generates gravity waves. Thus, it is necessary to minimize the reflection of gravity waves at the boundaries of the model domain. As a lateral boundary condition, we employ an extrapolation method of the Sommerfeld radiation condition proposed by Miller and Thorpe (1981). A local radiative upper boundary condition allowing for transmitting the wave energy has been proposed (Bougeault 1983; Klemp and Durran 1983). This radiation boundary condition was derived from a linear internal wave theory, but it was also effective in the nonlinear system (Klemp and Durran 1983). The boundary condition, in which the  $\phi$  field at the upper boundary is diagnostically determined from the Fourier transform of the  $w$  field at the boundary, is implemented in the model and is given by

$$\tilde{\phi} = \frac{N}{|k_h|} \tilde{w}, \quad (15)$$

where  $k_h$  is the wavenumber in the  $x$  direction. For the numerical calculation, the fast Fourier transform technique is used.

In order to reduce high-frequency numerical noise, a horizontal smoother of the fourth-order diffusion type (Perkey 1976) is applied. The numerical model has a domain size of 120 km in the horizontal and 3 km in the vertical. The horizontal and vertical grid sizes are 1 km and 100 m, respectively. The time step is 20 s.

### 3. Results and discussion

For both analytic and numerical models, we specify  $U_0 = 3 \text{ m s}^{-1}$  (unless otherwise mentioned),  $x_1 = 10 \text{ km}$ ,  $x_2 = 5x_1$ ,  $h = 1 \text{ km}$ , and  $T_0 = 15^\circ\text{C}$ . These and other parameters may be more suitable for a heated island surrounded by a warm ocean than for an urban heat island. However, we can easily choose a parameter set appropriate for an urban heat island, and the basic response features of a stably stratified atmosphere to low-level heating presented below are the same for both cases. The value of the heating top height ( $h = 1 \text{ km}$ ) can be considered as an approximate depth of the planetary boundary layer in which turbulent transport of heat associated with the heat island phenomenon mainly occurs. For the numerical simulations,  $\theta_0$  is

given by  $\theta_{00} \exp(N^2 z/g)$ , where  $\theta_{00}$  is the basic-state potential temperature at the surface and is set to  $T_0$ . Note that the analytic solutions for  $w$  and  $u$  [see Eqs. (13) and (14)] do not require information on  $\theta_0$ .

### a. Analytic solutions

Figure 1 shows the perturbation velocity and nonlinearity fields obtained from the analytic solutions for  $N = 0.01 \text{ s}^{-1}$ ,  $q_0 = 0.1 \text{ J kg}^{-1} \text{ s}^{-1}$ , and  $U_1 = 6 \text{ m s}^{-1}$  (basic horizontal wind at the height of 3 km). The nonlinearity parameter  $\mu$  is defined by  $|u(x, z)/U(z)|$ , that is, absolute value of the ratio of perturbation horizontal wind and basic wind. Equations (13) and (14) indicate that  $w$  and  $u$  are directly proportional to the heating amplitude  $q_0$ . Therefore, we can control  $q_0$  to make the linear assumption valid. Figures 1a and 1b exhibit the bands of positive and negative velocity perturbations with an upstream phase tilt, implying an upward energy transfer. This is a typical phenomenon that gravity waves generated by the local heat source in the presence of environmental flow produce. In the heating region, perturbation pressure becomes negative through the hydrostatic balance. So, an air parcel moving toward (away from) the strong heating zone centered at  $x = 0 \text{ km}$  in the lower atmosphere experiences acceleration (deceleration). Accordingly, there is a horizontal divergence (convergence) region on the upstream (downstream) side. This divergence (convergence) produces downward (upward) motion on the upstream (downstream) side of the heat island (Fig. 1a). This is consistent with the previous studies mentioned in the Introduction. The nonlinearity field (Fig. 1d) indicates that the linear assumption is valid for the given parameters except for the near-surface region near the heating center and on the downstream portion where  $\mu$  is as large as 0.5.

Recently, Lin and Chun (1991) showed from a scale analysis of the governing equations that a nonlinearity factor of the thermally induced finite-amplitude waves in a constant shear flow with a critical level is given by  $gq_0 L (c_p T_0 N U_s^2)^{-1}$ , where  $L$  is the characteristic horizontal length scale of the diabatic forcing and  $U_s$  the magnitude of the basic flow at the surface. Following their procedure, a nonlinearity factor in the present case with the constant shear flow without a critical level [see Eq. (5)] can be shown to be

$$\mu' = \frac{gq_0 L}{c_p T_0 N U_m^2}, \quad (16)$$

where  $U_m$  is the basic-state horizontal wind speed at the domain top height. The expression for  $\mu'$  has the same form as that of Lin and Chun (1991) except that  $U_s$  is replaced by  $U_m$ . The above equation indicates that the amplitude of the thermally induced wave is proportional to the amplitude and horizontal length scale of the heating and inversely proportional to the Brunt–Väisälä frequency and square of the basic-state

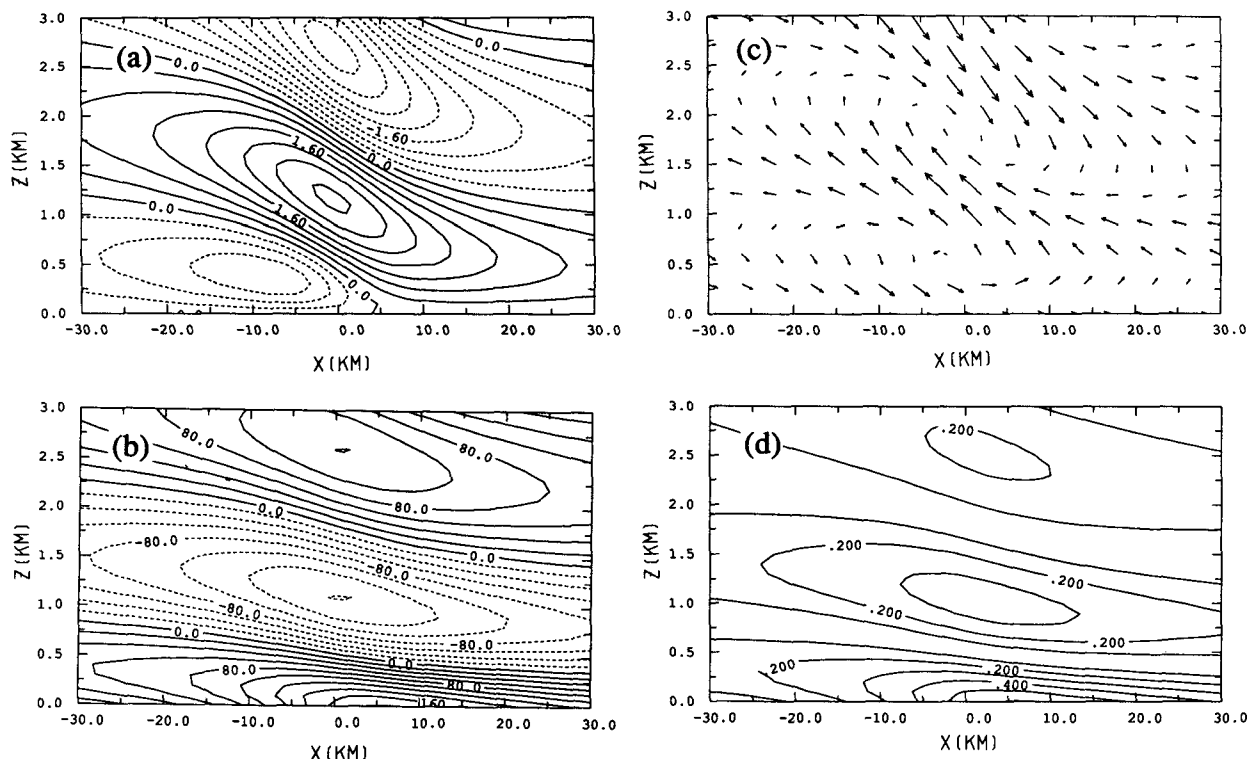


FIG. 1. Perturbation fields of (a) vertical velocity (contour interval of  $0.4 \text{ cm s}^{-1}$ ), (b) horizontal velocity (contour interval of  $20 \text{ cm s}^{-1}$ ), (c) velocity vector, and (d) field of the nonlinearity (contour interval of 0.1) for  $N = 0.01 \text{ s}^{-1}$ ,  $q_0 = 0.1 \text{ J kg}^{-1} \text{ s}^{-1}$ , and  $U_1 = 6 \text{ m s}^{-1}$  in the analytic solutions. In (c), the vertical component of velocity is exaggerated by a factor of 50.

wind at the domain top height. The value of the computed  $\mu'$  with the parameters used in Fig. 1 and  $L = 20 \text{ km}$  ( $2x_1$ ) is 0.19, implying that the assumption of the small-amplitude perturbation is valid for Fig. 1.

To investigate the effects of changes in basic-state stability and wind shear on circulation pattern, we plot the perturbation vertical velocity fields for  $N = 0.015 \text{ s}^{-1}$  (Fig. 2a) and  $U_1 = 9 \text{ m s}^{-1}$  (Fig. 2b). Other parameters specified are the same as those in Fig. 1. Figures 1a and 2 point out that the vertical wavelength becomes small as the stability of the mean flow increases and the basic-state wind speed at the model top (hence, the vertical wind shear in this case) decreases. This is because the vertical wavelength  $\lambda_z$  is proportional to the basic-state wind speed and inversely proportional to the Brunt-Väisälä frequency [ $\lambda_z = 2\pi U(z)/N$ ]. The values of the maximum downdraft and updraft of the first and second bands from the surface in Fig. 2a ( $-0.70$  and  $1.71 \text{ cm s}^{-1}$ , respectively) are much different from those in Fig. 1a ( $-1.52$  and  $2.88 \text{ cm s}^{-1}$ ), while the values in Fig. 2b ( $-1.49$  and  $2.92 \text{ cm s}^{-1}$ ) are similar to those in Fig. 1a.

Gravity waves can transport momentum and energy in the horizontal and vertical from one region to another. To get some insight into this effect, the vertical flux of integrated horizontal momentum divided by the basic-state density is calculated using

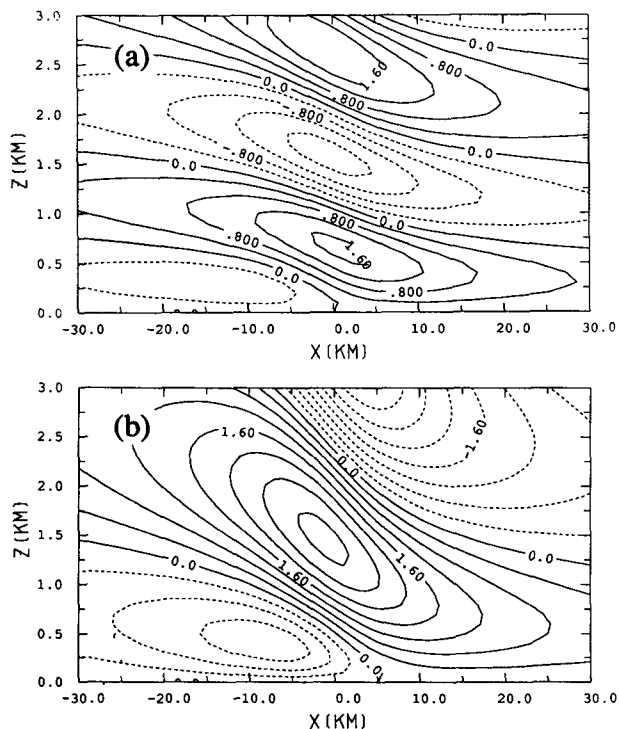


FIG. 2. Same as in Fig. 1a except for (a)  $N = 0.015 \text{ s}^{-1}$  and (b)  $U_1 = 9 \text{ m s}^{-1}$ .

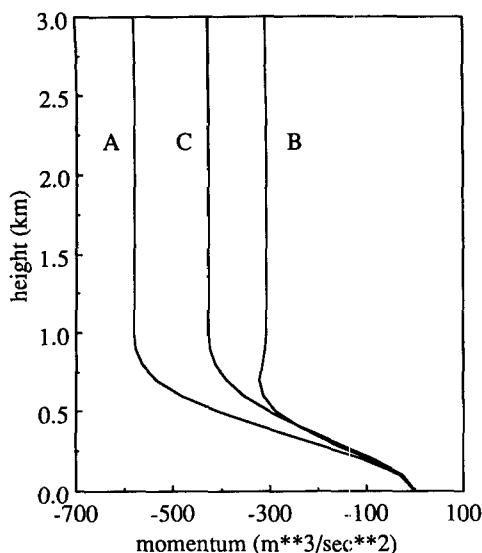


FIG. 3. Profile of the vertical flux of integrated horizontal momentum divided by the basic-state density  $M$  for the flow fields corresponding to Fig. 1 (A), Fig. 2a (B), and Fig. 2b (C).

$$M(z) = \int_{-\infty}^{\infty} u w dx. \quad (17)$$

Figure 3 shows the  $M$  profile for the three cases mentioned above. In each case, the momentum flux is zero at the surface because of zero perturbation vertical velocity there; above the surface, it takes a negative value with gradually increasing magnitude with height, and then has a constant negative value above the heating top height (1 km). The magnitude of the momentum flux in B, corresponding to Fig. 2a, is smaller than that in A (or C), corresponding to Fig. 1 (or Fig. 2b), due to the smaller perturbation velocity resulting from the larger Brunt-Väisälä frequency (Fig. 2a). The constancy of the momentum flux above the heating top height can be explained by a wave energy equation. Using Eqs. (1)–(4) under the assumption of steady-state and small-amplitude perturbation, one can derive a wave energy equation

$$\frac{\partial}{\partial x} (E_T U + \phi u) + \frac{\partial}{\partial z} (\phi w) = \frac{g^2}{c_p T_0 N^2} \frac{\theta q}{\theta_0} - u w \frac{dU}{dz}, \quad (18)$$

where  $E_T$  is the perturbation wave energy per unit mass defined by

$$E_T = \frac{1}{2} \left[ u^2 + \left( \frac{g \theta}{N \theta_0} \right)^2 \right]. \quad (19)$$

The  $E_T$  consists of a kinetic energy part and an available potential energy part. In an absence of diabatic forcing, the term  $-u w dU/dz$  in Eq. (18) (a conversion of kinetic energy of the basic flow) is a source of wave energy as described by Eliassen and Palm (1960). Integration of Eq. (18) from  $x = -\infty$  to  $\infty$  gives

$$\frac{d}{dz} \int_{-\infty}^{\infty} \phi w dx = \frac{g^2}{c_p T_0 N^2 \theta_0} \int_{-\infty}^{\infty} \theta q dx - M \frac{dU}{dz}. \quad (20)$$

Integrating the horizontal momentum equation multiplied by  $(Uu + \phi)$  from  $x = -\infty$  to  $\infty$  gives

$$\int_{-\infty}^{\infty} \phi w dx = -UM. \quad (21)$$

Substitution of Eq. (21) into Eq. (20) yields an expression for the vertical variation of  $M$

$$\frac{dM}{dz} = - \frac{g^2}{c_p T_0 N^2 \theta_0 U} \int_{-\infty}^{\infty} \theta q dx. \quad (22)$$

The above equation shows that the vertical flux of integrated horizontal momentum divided by the basic-state density  $M$  does not change with height in the adiabatic region (Eliassen and Palm 1960). Equation (21) indicates that the vertical flux of integrated wave energy is positive for all levels except for the surface because  $U$  is positive and  $M$  is negative in our cases (Fig. 3), implying an upward energy propagation.

To compare the flow response field in the shear-flow case with that in a uniform-flow case, the perturbation vertical velocity field in a uniform basic flow is analytically obtained by following the procedure described in section 2a. Thus,

$$w(x, z) = \frac{g q_0 x_1}{c_p T_0 N^2} \left[ \left( \frac{x_1}{x^2 + x_1^2} - \frac{x_2}{x^2 + x_2^2} \right) \left( 1 - \frac{z}{h} - \cos \delta z + \frac{\cos \delta h}{\delta h} \sin \delta z \right) + \left( \frac{x}{x^2 + x_1^2} - \frac{x}{x^2 + x_2^2} \right) \left( 1 - \frac{\sin \delta h}{\delta h} \right) \sin \delta z \right] \quad \text{for } 0 \leq z \leq h, \quad (23a)$$

$$w(x, z) = \frac{g q_0 x_1}{c_p T_0 N^2} \left( 1 - \frac{\sin \delta h}{\delta h} \right) \left[ - \left( \frac{x_1}{x^2 + x_1^2} - \frac{x_2}{x^2 + x_2^2} \right) \cos \delta z + \left( \frac{x}{x^2 + x_1^2} - \frac{x}{x^2 + x_2^2} \right) \sin \delta z \right] \quad \text{for } z > h, \quad (23b)$$

where  $U_c$  is the basic-state horizontal wind speed of a positive constant and  $\delta = N/U_c$ . Figure 4 shows the perturbation vertical velocity field for  $U_c = 4.5 \text{ m s}^{-1}$ , while the other parameters were kept the same as those

corresponding to Fig. 1. This value of  $U_c$  is equal to the height-averaged basic-state wind in Fig. 1. A comparison of Fig. 4 with Fig. 1a indicates that the char-

acteristic flow pattern in the uniform flow is similar to that in the shear flow without a critical level. However, the magnitude of the perturbation is much larger in the shear-flow case than in the uniform flow case, especially in the second and third bands from the surface. The larger perturbation in the shear flow case is because the basic-state wind shear is a source of the perturbation wave energy [see Eq. (18)]. When there is no environmental flow, it follows from the thermodynamic energy equation that  $w(x, z) = gq(c_p T_0 N^2)^{-1}$ ; that is,

$$u(x, z) = \frac{gq_0 x_1}{c_p T_0 N^2} \left[ \left( \arctan \frac{x}{x_1} - \arctan \frac{x}{x_2} \right) \left( \frac{1}{h} - \delta \sin \delta z - \frac{\cos \delta h}{h} \cos \delta z \right) - \frac{1}{2} \left( \ln \frac{x^2 + x_1^2}{x^2 + x_2^2} \right) \delta \left( 1 - \frac{\sin \delta h}{\delta h} \right) \cos \delta z \right] \quad \text{for } 0 \leq z \leq h, \quad (24a)$$

$$u(x, z) = \frac{gq_0 x_1}{c_p T_0 N^2} \left( 1 - \frac{\sin \delta h}{\delta h} \right) \left[ - \left( \arctan \frac{x}{x_1} - \arctan \frac{x}{x_2} \right) \delta \sin \delta z - \frac{1}{2} \left( \ln \frac{x^2 + x_1^2}{x^2 + x_2^2} \right) \delta \cos \delta z \right] \quad \text{for } z > h. \quad (24b)$$

At the center of the diabatic forcing, both Eqs. (24a) and (24b) reduce to a single equation of

$$u(0, z) = \frac{gq_0 x_1}{c_p T_0 N^2} \delta \left( 1 - \frac{\sin \delta h}{\delta h} \right) \left( \ln \frac{x_2}{x_1} \right) \cos \delta z. \quad (25)$$

Since the basic-state wind  $U_c$  and  $(1 - \sin \delta h / \delta h)$  are positive and  $x_1 < x_2$ ,  $u(0, z)$  has a minimum value when

$$\cos \delta z = -1. \quad (26)$$

Therefore, the height of maximum possible steepening is represented by

$$z_n = \frac{(2n+1)\pi}{\delta} = \frac{(2n+1)\pi U_c}{N}, \quad n = 0, 1, 2, 3, \dots \quad (27)$$

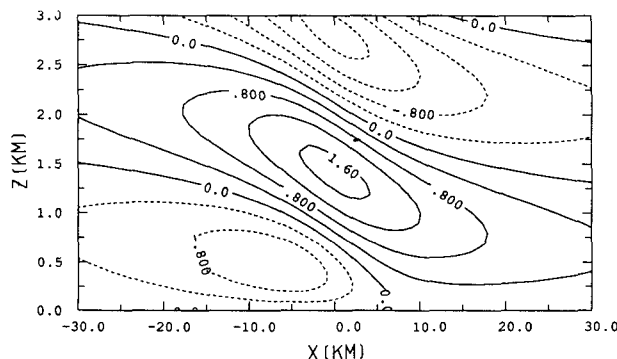


FIG. 4. Same as in Fig. 1a except for a constant basic-state wind of  $U_c = 4.5 \text{ m s}^{-1}$ .

the perturbation vertical velocity is proportional to the diabatic heating and inversely proportional to the square of the Brunt-Väisälä frequency.

A critical steepness of streamfunction can occur when  $u + U = 0$ . An overturning of streamfunction is possible when  $u$  and  $U$  are in opposite signs and  $|u| > |U|$ , while the steepness is less than a critical steepness when  $u$  and  $U$  are in opposite signs and  $|u| < |U|$ . To study the steepness in the uniform flow (Chun 1991), the perturbation horizontal velocity field is obtained using Eqs. (14) and (23):

With  $N = 0.01 \text{ s}^{-1}$  and  $U_c = 4.5 \text{ m s}^{-1}$ , the computed  $z_0$  and  $z_1$  are 1414 and 4241 m, respectively. The heating amplitude at the critical steepening height ( $u + U = 0$  at  $x = 0$  and  $z = z_n$ ) can be expressed by

$$q_{0c} = c_p T_0 N U_c^2 \left[ g x_1 \left( 1 - \frac{\sin \delta h}{\delta h} \right) \left( \ln \frac{x_2}{x_1} \right) \right]^{-1}. \quad (28)$$

Note that the linear assumption breaks down in the regions where the magnitude of perturbation horizontal velocity is comparable to (or greater than) the magnitude of basic-state wind. For the parameter set used in Fig. 4 except for  $q_0$ , the calculated  $q_{0c}$  is  $0.38 \text{ J kg}^{-1} \text{ s}^{-1}$ . Figure 5 shows the total streamfunction  $\psi_T$  field for  $q_0 = 0.3$  and  $0.8 \text{ J kg}^{-1} \text{ s}^{-1}$ . The other parameters specified are the same as those in Fig. 4. The  $\psi_T$  is obtained analytically using

$$\psi_T = U_c z - \int_{-\infty}^x w dx. \quad (29)$$

The first and second terms on the right-hand side of the above equation represent the mean and perturbation streamfunction, respectively. When the heating amplitude is less than the critical value ( $q_{0c} = 0.38 \text{ J kg}^{-1} \text{ s}^{-1}$ ), the angle of the steepening is less than  $90^\circ$  (Fig. 5a). On the other hand, there is an overturning of streamfunction in the case of  $q_0 > q_{0c}$  near the maximum possible steepening height of  $z_0 = 1414 \text{ m}$  (Fig. 5b).

An internal gravity wave passing through a stably stratified fluid experiences a dramatic change at a critical level. It has been shown in the linear theories (Booker and Bretherton 1967; Lin 1987; Lin and Chun 1991) that the gravity wave is attenuated exponentially

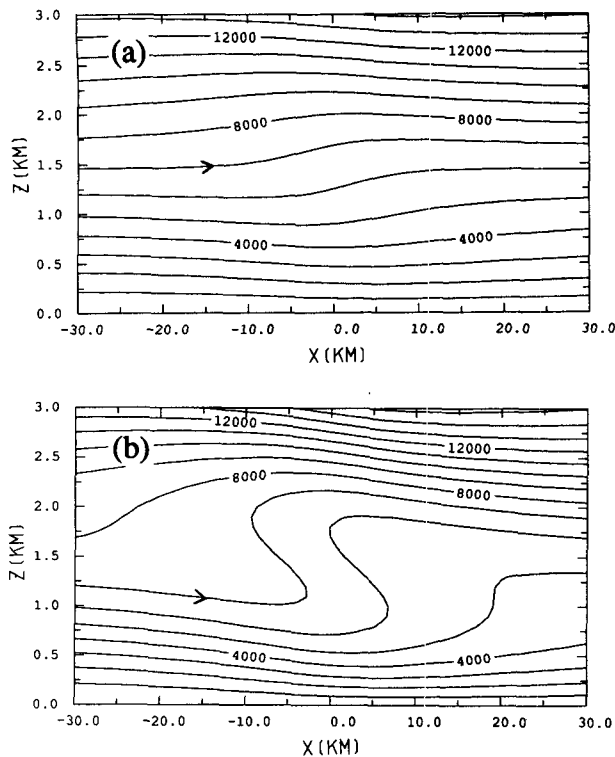


FIG. 5. Total streamfunction field for  $q_0 =$  (a) 0.3 and (b) 0.8  $\text{J kg}^{-1} \text{s}^{-1}$ , while the other parameters were kept the same as those in Fig. 4. The contour interval is  $1000 \text{ m}^2 \text{s}^{-1}$ .

as it propagates through a critical level when the  $Ri$  is everywhere larger than  $1/4$ . However, the nonlinearity becomes important near the critical level. In a nonlinear numerical model study of critical levels for internal gravity waves, Breeding (1971) found that a large portion of the incident waves is reflected for a relatively small value of  $Ri$ , while the flow response is similar to the linear flow response for a large value of  $Ri$ . Using a nonlinear numerical model, Clark and Peltier (1984) examined critical-level reflection and the resonant growth of nonlinear mountain waves. They showed that when the critical level is located near certain discrete heights above ground, the incident and reflected waves interfere constructively and the wave amplitude in the low levels is resonantly enhanced. Although an investigation of the critical level effect in the present heat island problem is not a purpose of this study, an interesting research area would be to examine the effect of a critical level on thermally induced finite-amplitude waves in connection with the steepening heights discussed above, as Clark and Peltier (1984) did in the mountain wave problem.

### b. Numerical simulations

Before conducting nonlinear numerical simulations, linear model performance is evaluated. In a theoretical study on the transient dynamics of the airflow near a

local heat source, Lin and Smith (1986) pointed out the lack of a steady-state solution in the linear, inviscid flow system without the widespread cooling term. Although in the present study the widespread cooling term is included and the integration of the heating function from  $x = -\infty$  to  $\infty$  at any level is zero, there is net heating at any level of the forcing region resulting from the finite model domain. We remedy this by adding the Rayleigh friction and the Newtonian cooling terms ( $-\nu u$  and  $-\nu \theta$ ) to the horizontal momentum equation and the thermodynamic energy equation, respectively.

Figure 6 shows the time evolution of the maximum perturbation horizontal wind speed with different values of  $\nu$  for  $N = 0.01 \text{ s}^{-1}$ ,  $q_0 = 0.1 \text{ J kg}^{-1} \text{s}^{-1}$ , and  $U_1 = 6 \text{ m s}^{-1}$ . Even though the linear model in the inviscid flow is integrated up to 30 h, the numerical solution still exhibits a gradually increasing tendency until the end of the time integration and does not reach any quasi-steady state (A). Sensitivity tests to choose an appropriate value of the coefficient  $\nu$  for the present model show that the maximum perturbation horizontal wind becomes weaker as  $\nu$  is increased. With a value of  $\nu = 10^{-5} \text{ s}^{-1}$  (B), the maximum  $u$  continues to increase with time, although the rate of increase is small compared with that in the inviscid case (A). This is also true for the case with  $\nu = 2.5 \times 10^{-5} \text{ s}^{-1}$  (C). With a value of  $\nu = 10^{-4} \text{ s}^{-1}$  (E), a quasi-steady state is achieved after about 6 h of integration, but the magnitude of the maximum  $u$  is too small compared with that in the analytic solution. A value of  $\nu = 5 \times 10^{-5} \text{ s}^{-1}$  (D), which gives an  $e$ -folding time of 5.6 h, yields a quasi-steady state after about 12 h of integration and a closer approach to the analytic solution than in the case E. A properly chosen value of  $\nu$  between  $2.5 \times 10^{-5}$  and  $5 \times 10^{-5} \text{ s}^{-1}$  may yield more accurate numerical solutions than in the case with  $\nu = 5 \times 10^{-5} \text{ s}^{-1}$ , but it will take more than 0.5 day to reach a quasi-steady state. It is necessary to obtain quasi-steady numerical

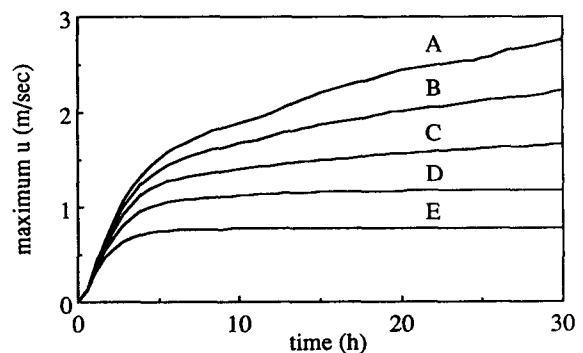


FIG. 6. Time evolution of the maximum perturbation horizontal wind speed for  $\nu = 0$  (A),  $10^{-5}$  (B),  $2.5 \times 10^{-5}$  (C),  $5 \times 10^{-5}$  (D), and  $10^{-4}$  (E)  $\text{s}^{-1}$  in the linear numerical model simulations. The  $\nu$  is the coefficient of the Rayleigh friction and the Newtonian cooling. The specified parameters are  $N = 0.01 \text{ s}^{-1}$ ,  $q_0 = 0.1 \text{ J kg}^{-1} \text{s}^{-1}$ , and  $U_1 = 6 \text{ m s}^{-1}$ .



solutions within 0.5 day, because the time scale of the heat island phenomenon over a warm ocean is about 0.5 day (from sunrise to sunset).

The nonlinear numerical model with  $\nu = 0$  and  $5 \times 10^{-5} \text{ s}^{-1}$  for  $N = 0.01 \text{ s}^{-1}$ ,  $q_0 = 0.1 \text{ J kg}^{-1} \text{ s}^{-1}$ , and  $U_1 = 6 \text{ m s}^{-1}$  is integrated up to 30 h. The time evolution of the maximum  $u$  in the inviscid case (A in Fig. 7) shows a quasi-steady state after about 20 h of integration with a slightly decreasing tendency of the maximum  $u$  after about 24 h. An earlier quasi steadiness could be obtained by including the  $-\nu u$  and  $-\nu \theta$  terms with  $\nu = 5 \times 10^{-5} \text{ s}^{-1}$  (B in Fig. 7). A close inspection of the linear (D in Fig. 6) and the corresponding nonlinear (B in Fig. 7) cases indicates that the value of the maximum  $u$  at the quasi-steady state in the linear simulation is slightly larger than that in the nonlinear simulation. For the reason mentioned above, the Rayleigh friction and the Newtonian cooling terms with  $\nu = 5 \times 10^{-5} \text{ s}^{-1}$  are incorporated in all the subsequent numerical model simulations.

To examine the effects of nonlinearity on the simulated flow field, nonlinear numerical experiments are performed over a wide range of heating amplitudes. Note that the nonlinearity factor  $\mu'$  is proportional to  $q_0$  [see Eq. (16)]. Figure 8 shows the simulated perturbation vertical velocity fields at 10 h for  $q_0 = 0.1, 0.3, 0.5, 0.7$ , and  $0.9 \text{ J kg}^{-1} \text{ s}^{-1}$  with  $N = 0.01 \text{ s}^{-1}$  and  $U_1 = 6 \text{ m s}^{-1}$ . As should be expected, the flow response pattern is similar to that in the linear case (Fig. 1a) when the heating amplitude (hence, the nonlinearity factor) is small. However, it gradually deviates from the linear gravity-wave response field as the heating amplitude becomes larger. As the heating amplitude increases, the updraft circulation cell on the downstream side strengthens and shifts farther downwind at  $t = 10 \text{ h}$ . In the linear case, the basic flow pattern is unchanged for every value of  $q_0$  (but the magnitude of perturbation is different) because the perturbation vertical velocity is directly proportional to the heating amplitude [Eq. (13)]. In the case of  $q_0 = 0.5(0.7)$

$\text{J kg}^{-1} \text{ s}^{-1}$ , the updraft circulation cell is located around  $x = 18(22) \text{ km}$  with a maximum vertical velocity of  $10(24) \text{ cm s}^{-1}$ .

To investigate whether the updraft circulation cell in Fig. 8e was physically induced or was generated as a result of gravity-wave reflection at the model lateral boundary, a numerical model experiment was performed in which the horizontal domain size was doubled, but the horizontal resolution was kept same. The results showed that the pattern and magnitude of the updraft circulation cell with time were very similar to those in the case of Fig. 8e, indicating that the results shown in Fig. 8 are not a result of boundary reflection.

Figure 9 shows the maximum positive perturbation vertical velocity at 10 h as a function of the heating amplitude. When  $q_0$  is smaller than about  $0.4 \text{ J kg}^{-1} \text{ s}^{-1}$ , the maximum updraft tends to increase linearly with  $q_0$ . On the other hand, above that value the maximum updraft increases exponentially with  $q_0$ . This figure implies that the linear dynamics can be applied to investigate flow characteristics past a heat island as long as the heat island intensity is weak enough. Increasing the horizontal model domain size would produce a very similar result to Fig. 9 because, as mentioned above, the updraft circulation cell on the downstream side was physically induced.

Using a three-dimensional mesoscale numerical model, Hjelmfelt (1982) studied urban effects on mesoscale boundary-layer vertical air motion. The higher urban surface roughness, which leads to low-level convergence and hence upward motion, and the urban heat island were found to be important factors for upward air motion downwind of the city. Surface roughness differences between land and ocean can influence airflow past a heated island over a warm ocean. Although the present model does not include the surface roughness effect, the result from the simple two-dimensional numerical model is consistent with that from the sophisticated three-dimensional numerical model (Hjelmfelt 1982). The observational study in the Barbados island region during summers (DeSouza 1972) showed the downward motion over the island and the upward motion on the downstream side with a maximum updraft of  $\sim 3.5 \text{ cm s}^{-1}$  at the height of  $\sim 0.6 \text{ km}$  off the leeward coast during the day. The vertical location and magnitude of the maximum updraft downwind in the case of Fig. 8b are similar to those in the Barbados case.

Observed precipitation enhancement on the downstream side of a heat island (e.g., Changnon 1972) was partly attributed to the gravity-wave-produced updraft in response to thermal forcing in the linear theoretical study (Lin and Smith 1986). This is true when the nonlinearity effect is small. However, the results from the nonlinear numerical simulations (Figs. 8 and 9) indicate that when the nonlinearity becomes larger, the updraft on the downstream side, which is stronger than the updraft predicted by the linear theory, is more fa-

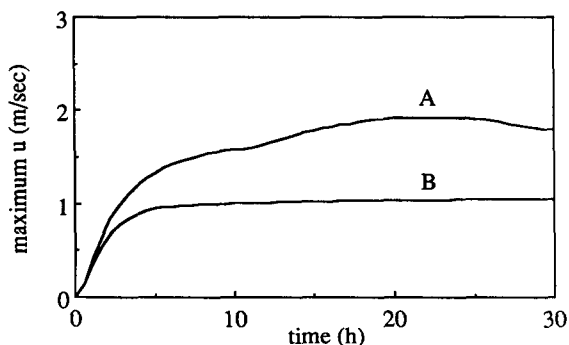


FIG. 7. Time evolution of the maximum perturbation horizontal wind speed for  $\nu = 0$  (A) and  $5 \times 10^{-5} \text{ s}^{-1}$  (B) in the nonlinear numerical model simulations. The specified parameters are  $N = 0.01 \text{ s}^{-1}$ ,  $q_0 = 0.1 \text{ J kg}^{-1} \text{ s}^{-1}$ , and  $U_1 = 6 \text{ m s}^{-1}$ .

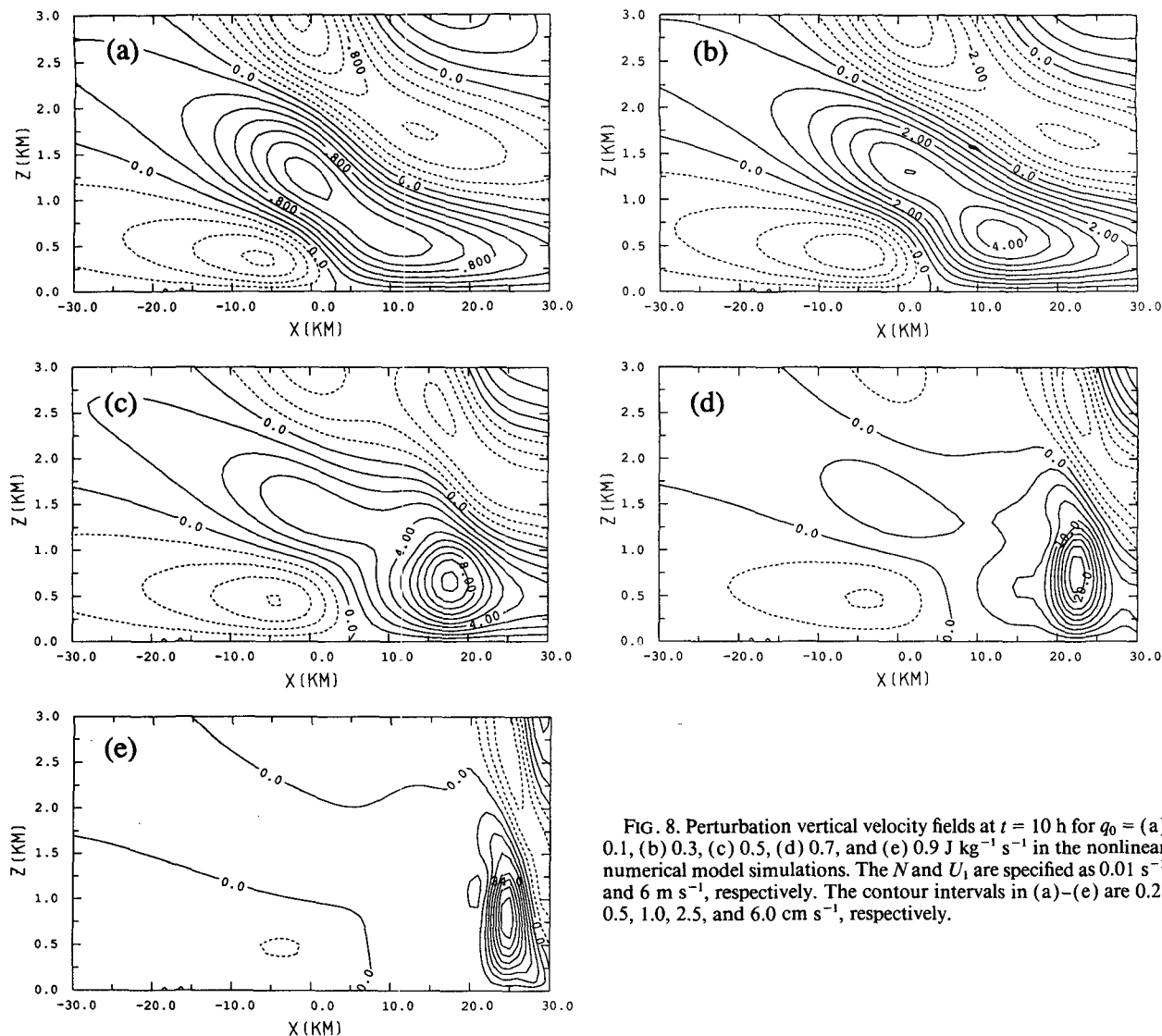


FIG. 8. Perturbation vertical velocity fields at  $t = 10$  h for  $q_0 =$  (a) 0.1, (b) 0.3, (c) 0.5, (d) 0.7, and (e)  $0.9 \text{ J kg}^{-1} \text{ s}^{-1}$  in the nonlinear numerical model simulations. The  $N$  and  $U_1$  are specified as  $0.01 \text{ s}^{-1}$  and  $6 \text{ m s}^{-1}$ , respectively. The contour intervals in (a)–(e) are 0.2, 0.5, 1.0, 2.5, and  $6.0 \text{ cm s}^{-1}$ , respectively.

avorable for convection, hence precipitation enhancement. Also, the numerical model results indicate that the convective activity region due to the updraft can shift farther downwind as the nonlinearity becomes larger. Note that we investigated the nonlinear effect by changing the heating amplitude with the other parameters held fixed in  $\mu'$  [see Eq. (16)]. Thus, these results are valid for the sensitivity of nonlinear flow response to  $q_0$ . Recently, Changnon et al. (1991) analyzed precipitation events in the St. Louis area using the data from a circular, dense, raingage network and the available wind data. They found a 17% increase during fall and a 4% increase during spring in precipitation downwind of St. Louis. An interesting research area would be to observationally document the intensity and location of precipitation in connection with heat island intensity and qualitatively compare results with the analyses based on the present study (Figs. 8 and 9).

Figure 8 shows that on the upstream side of the heat island the perturbation vertical velocity field for larger heating amplitude still exhibits characteristics of the linear gravity-wave-produced updraft and downdraft. To clarify this, the vertical motion field on a portion of the domain for  $q_0 = 0.9 \text{ J kg}^{-1} \text{ s}^{-1}$  (Fig. 8e) is reproduced with a contour interval of  $1 \text{ cm s}^{-1}$  in Fig. 10. This figure clearly indicates that the flow pattern on the upstream side is similar to that produced by the gravity wave in response to the thermal forcing. Therefore, for larger heating amplitude there are two distinct flow features: the gravity-wave-type response on the upstream side of the heat island and the strong updraft circulation cell located on the downstream side.

For the purpose of investigating the transient behavior of the updraft circulation cell downwind of the heat island, the time evolutions of the location of the maximum updraft from the maximum heating center and the maximum updraft in the case of  $q_0$

$= 0.7 \text{ kg}^{-1} \text{ s}^{-1}$  are plotted in Fig. 11. The maximum updraft increases rapidly during the first 3 h and tends to decrease gradually up to 8 h. The updraft cell originates from the region of the maximum heating and propagates downwind up to 7 h. After about 8 h, the updraft cell tends to be quasi-stationary in both location and strength until the end of the integration (10 h). This implies that the advection terms, horizontal pressure gradient force term, and viscous terms are approximately balanced in each portion of the updraft cell in this particular case. To examine whether the updraft cell in this case can move farther downwind, the numerical model integration was continued up to 20 h. The result (not shown here) showed that the updraft cell does not move farther downwind, but strengthens.

A numerical experiment is performed in which the basic-state horizontal wind speed at every level is increased by  $1 \text{ m s}^{-1}$  by setting  $U_0 = 4 \text{ m s}^{-1}$  and  $U_1 = 7 \text{ m s}^{-1}$  in the previous case. This simulation is chosen to see whether the increased basic wind can cause continuous movement of the updraft cell downwind of the heat island. Figure 12 shows the time evolution of the location of the maximum updraft associated with the updraft cell downwind in this case. This figure indicates that the updraft cell continues to move downwind because of the larger advection effect and reaches the model right boundary at about 10 h. Examination of the time series of the perturbation vertical velocity field during the 20-h period (not shown here) revealed that the updraft cell just passed through the model boundary at about 11 h without any significant reflection of  $w$  at the lateral boundary. Figures 11 and 12 imply that the continuing propagation of the updraft circulation cell on the downstream side of the heat island is related to basic-state wind speed.

Figure 13 shows the profiles of the perturbation po-

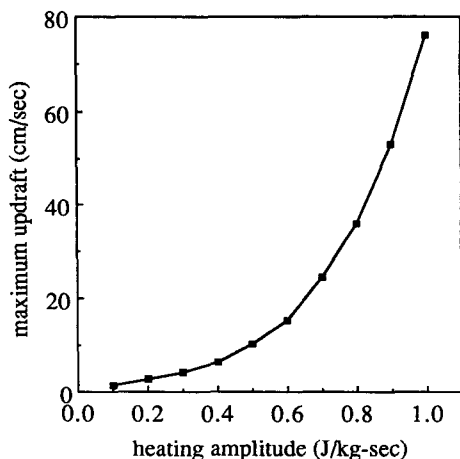


FIG. 9. Maximum positive perturbation vertical velocity at  $t = 10$  h as a function of the heating amplitude (from  $q_0 = 0.1$  to  $1.0 \text{ J kg}^{-1} \text{ s}^{-1}$  with an increment of  $0.1 \text{ J kg}^{-1} \text{ s}^{-1}$ ) in the nonlinear numerical model simulations. The  $N$  and  $U_1$  are specified as  $0.01 \text{ s}^{-1}$  and  $6 \text{ m s}^{-1}$ , respectively.

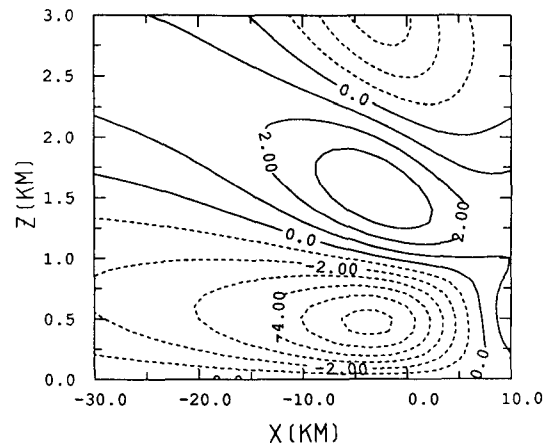


FIG. 10. Same as in Fig. 8e except for a domain portion of Fig. 8e with a contour interval of  $1 \text{ cm s}^{-1}$ .

tential temperature and the Richardson number for the total (basic plus perturbation) flow field at  $x = 10 \text{ km}$  in the case of Fig. 8b ( $q_0 = 0.3 \text{ J kg}^{-1} \text{ s}^{-1}$ ). The perturbation potential temperature is positive up to  $z = 0.9 \text{ km}$  with a maximum value of  $0.72 \text{ K}$  at the height of  $0.3 \text{ km}$  and then it is negative. Above  $2.3 \text{ km}$  height, it is positive again. The calculated  $Ri$  is larger than 5 everywhere, indicating that the buoyancy term is dominant over the shear term. Around  $z = 0.9 \text{ km}$  and above  $z = 2.2 \text{ km}$ ,  $Ri$  is larger than 100. This is because the vertical wind shear in those regions is very weak compared with the other regions at  $x = 10 \text{ km}$ .

#### 4. Summary and conclusions

Airflow characteristics past a heat island have been investigated using both a linear analytic model and a nonlinear numerical model in the context of the response of a stably stratified atmosphere to specified low-level thermal forcing. For this purpose, a two-dimensional, incompressible, hydrostatic, nonrotating, Boussinesq airflow system was employed. The basic-state horizontal wind was assumed to increase linearly with height without a wind-reversal level. The heating

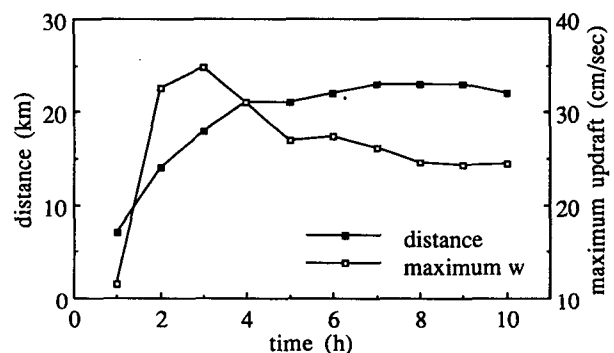


FIG. 11. Time evolutions of the location of the maximum positive vertical velocity from the maximum heating center ( $x = 0 \text{ km}$ ) and the maximum positive vertical velocity in the case of  $q_0 = 0.7 \text{ J kg}^{-1} \text{ s}^{-1}$  (corresponding to Fig. 8d).

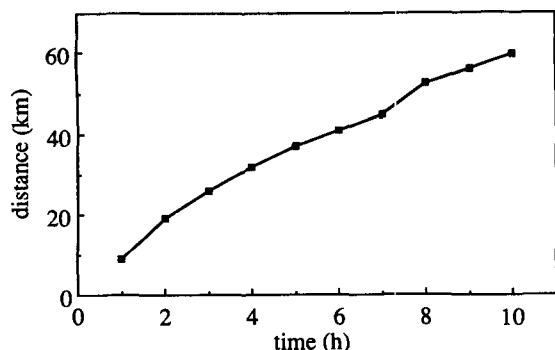


FIG. 12. Time evolution of the location of the maximum positive vertical velocity associated with the updraft circulation cell downwind of the heat island. All the specified parameters are the same as those in Fig. 8d except for  $U_0 = 4 \text{ m s}^{-1}$  and  $U_1 = 7 \text{ m s}^{-1}$ .

was specified as a bell-shaped function in the horizontal and as decreasing linearly with height up to a certain level and zero above that level.

The flow response fields obtained from the steady-state, linear, analytic solutions exhibit bands of positive and negative velocity perturbations with an upstream phase tilt. The air parcel descends over the heat island and ascends on the downstream side. The vertical wavelength becomes small as the stability of the mean flow increases and the basic wind speed at the domain top height decreases. These results are similar to previous studies. Following Lin and Chun's (1991) scale analysis of the governing equations, a nonlinearity factor of the thermally induced finite-amplitude waves was shown to be proportional to the amplitude and horizontal length scale of the heating and inversely proportional to the Brunt-Väisälä frequency and square of the basic-state wind at the domain top height. The calculated vertical flux of integrated horizontal momentum divided by the basic-state density is zero at the surface, takes a negative value with gradually increasing magnitude with height, and then has a constant negative value above the heating top height (implying an upward energy propagation).

The result from the constant shear-flow case was compared with that from the uniform basic flow case. The characteristic flow pattern is similar to each other. However, the magnitude of the perturbation is much larger in the shear flow than in the uniform flow. This is because the basic-state wind shear is a source of the perturbation wave energy. The height of maximum possible steepening and the heating amplitude at the critical steepening height were analytically obtained in the uniform basic-state wind case. When the heating amplitude is greater than the critical value, an overturning of streamfunction takes place near the maximum possible steepening height.

The result from the linear numerical model simulation in the inviscid flow showed the lack of simulated quasi-steady-state solutions. This is because of the

presence of the net heating at any level of the heating region resulting from the finite model domain in the present study. To obtain quasi-steady-state numerical solutions, the Rayleigh friction and the Newtonian cooling terms with a carefully chosen value of  $\nu$  were added to the horizontal momentum equation and the thermodynamic energy equation, respectively.

The effects of nonlinearity on the simulated flow pattern were examined through the nonlinear numerical model simulations over a wide range of heating amplitudes. For smaller heating amplitude (hence, smaller nonlinearity factor), the flow response field is similar to the linear gravity-wave-produced flow response field. On the other hand, for larger heating amplitude (hence, larger nonlinearity factor) there are two distinct features of flow response: the gravity-wave-type response field on the upstream side of the heat island and the strong updraft circulation cell located on the downstream side. As the heating amplitude increases, the updraft cell strengthens and shifts farther downwind. The updraft cell produced by the nonlinear processes is believed to be partly responsible for precipitation enhancement observed on the downstream side of the heat island. The numerical experiment with the increased basic-state wind speed at every level in the case with the larger heating amplitude revealed that the updraft circulation cell on the downstream side of the heat island continues to propagate downwind within the present model framework. This implies that the continuing downwind propagation of the updraft circulation cell is related to basic-state wind speed.

In the real atmosphere, the heat source region of a heated island, in an urban or sea setting, is located at (or near) the surface and the heat is transported from

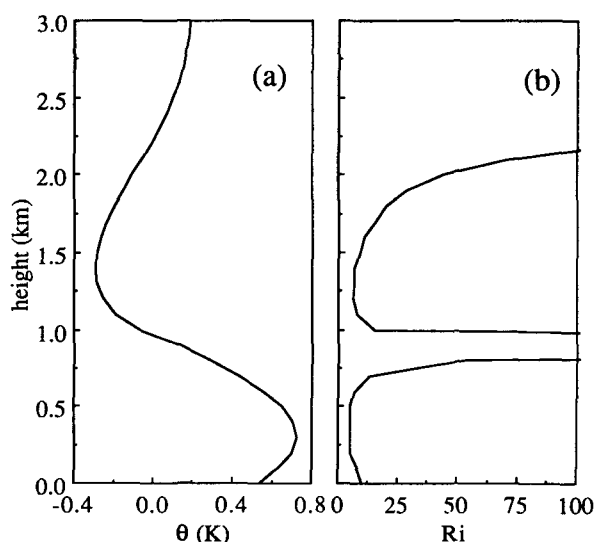


FIG. 13. Profiles of (a) the perturbation potential temperature and (b) the Richardson number for the total flow field at  $x = 10 \text{ km}$  in the case of Fig. 8b. In (b), the regions with the Richardson number larger than 100 are not plotted for the clarity of the figure.

the surface into the atmosphere primarily by turbulent thermal diffusion processes. Therefore, to properly represent and understand this mechanism, numerical models with detailed planetary boundary layer physics with surface energy budget equation would be more appropriate than the present model with the specified heating distribution. Two examples with detailed boundary-layer physics are the three-dimensional mesoscale model to simulate the effects of the city on boundary-layer airflow and vertical air motion (Hjelmfelt 1982) and the two-dimensional mesoscale model to simulate the urban mixed layer (Byun 1987). The current numerical model neglected earth's rotational and nonhydrostatic effects. The hydrostatic approximation is valid for the horizontal heating length scale of  $\sim 20$  km (Hsu 1987). However, earth's rotation can have some influence on the flow variables (Olfe and Lee 1971) because the calculated Rossby number with  $U \sim 4.5$  m s $^{-1}$ ,  $f \sim 5 \times 10^{-5}$  s $^{-1}$ , and  $L \sim 20$  km is 4.5. In spite of its simplicity, the present numerical model still can provide some insight into the basic dynamics of flow field past a heat island.

**Acknowledgments.** The author would like to thank Hye-Yeong Chun, Mark DeMaria, Yuh-Lang Lin and three anonymous reviewers for providing valuable comments on this study. This research was partially supported by NASA under RTOP 461-53-51.

#### REFERENCES

- Angell, J. K., D. H. Pack, C. R. Dickson, and W. H. Hoecker, 1971: Urban influence on nighttime airflow estimated from tethered flights. *J. Appl. Meteor.*, **10**, 194–204.
- Booker, J. R., and F. P. Bretherton, 1967: The critical layer for internal gravity waves in a shear flow. *J. Fluid Mech.*, **27**, 513–539.
- Bougeault, P., 1983: A non-reflective upper boundary condition for limited-height hydrostatic models. *Mon. Wea. Rev.*, **111**, 420–429.
- Breeding, R. J., 1971: A non-linear investigation of critical levels for internal atmospheric gravity waves. *J. Fluid Mech.*, **50**, 545–563.
- Byun, D.-W., 1987: A two-dimensional mesoscale numerical model of St. Louis urban mixed layer. Ph.D. thesis, North Carolina State University, Raleigh, 216 pp.
- Changnon, S. A., 1972: Urban effects on thunderstorm and hail storm frequencies. *Conf. Urban Environment*, Philadelphia, Amer. Meteor. Soc., 177–194.
- , R. T. Shealy, and R. W. Scott, 1991: Precipitation changes in fall, winter, and spring caused by St. Louis. *J. Appl. Meteor.*, **30**, 126–134.
- Chun, H.-Y., 1991: Role of a critical level in a shear flow with diabatic forcing. Ph.D. thesis, North Carolina State University, Raleigh, 159 pp.
- Clark, T. L., and W. R. Peltier, 1984: Critical level reflection and the resonant growth of nonlinear mountain waves. *J. Atmos. Sci.*, **41**, 3122–3134.
- DeSouza, R. L., 1972: A study of atmospheric flow over a tropical island. Dept. of Meteorology, Florida State University, Tallahassee, 203 pp.
- Eliassen, A., and E. Palm, 1960: On the transfer of energy in stationary mountain waves. *Geophys. Publ.*, **22**, 1–23.
- Garstang, M., P. D. Tyson, and G. D. Emmitt, 1975: The structure of heat islands. *Rev. Geophys. and Space Phys.*, **13**, 139–165.
- Hjelmfelt, M. R., 1982: Numerical simulation of the effects of St. Louis on mesoscale boundary-layer airflow and vertical air motion: Simulations of urban vs non-urban effects. *J. Appl. Meteor.*, **21**, 1239–1257.
- Hsu, H.-M., 1987: Study of linear steady atmospheric flow above a finite surface heating. *J. Atmos. Sci.*, **44**, 186–199.
- Klemp, J. B., and D. R. Durran, 1983: An upper boundary condition permitting internal gravity wave radiation in numerical mesoscale models. *Mon. Wea. Rev.*, **111**, 430–444.
- Lin, Y.-L., 1987: Two-dimensional response of a stably stratified shear flow to diabatic heating. *J. Atmos. Sci.*, **44**, 1375–1393.
- , and H.-Y. Chun, 1991: Effects of diabatic cooling in a shear flow with a critical level. *J. Atmos. Sci.*, **23**, 2476–2491.
- , and R. B. Smith, 1986: Transient dynamics of airflow near a local heat source. *J. Atmos. Sci.*, **43**, 40–49.
- Miller, M. J., and A. J. Thorpe, 1981: Radiation conditions for the lateral boundaries of limited-area numerical models. *Quart. J. Roy. Meteor. Soc.*, **107**, 615–628.
- Myrup, L. O., 1969: A numerical model of the urban heat island. *J. Appl. Meteor.*, **8**, 908–918.
- Navon, I. M., and H. A. Riphagen, 1979: An implicit compact fourth-order algorithm for solving the shallow-water equations in conservation-law form. *Mon. Wea. Rev.*, **107**, 1107–1127.
- Ogura, Y., and M.-T. Liou, 1980: The structure of a midlatitude squall line: A case study. *J. Atmos. Sci.*, **37**, 553–567.
- Oke, T. R., 1973: City size and the urban heat island. *Atmos. Environ.*, **7**, 769–779.
- Olfe, D. B., and R. L. Lee, 1971: Linearized calculations of urban heat island convection effects. *J. Atmos. Sci.*, **28**, 1374–1388.
- Perkey, D. J., 1976: A description and preliminary results from a fine-mesh model for forecasting quantitative precipitation. *Mon. Wea. Rev.*, **104**, 1513–1526.
- Smith, R. B., and Y.-L. Lin, 1982: The addition of heat to a stratified airstream with application to the dynamics of orographic rain. *Quart. J. Roy. Meteor. Soc.*, **108**, 353–378.